Facile synthesis of a TiO$_2$-Al$_2$O$_3$-GnPs compound and its application in the photocatalytic degradation of Diuron

Alina de J. Zurita-Yduarte [a], Diana J. Gallegos-Hernández [a], Uriel A. Sierra-Gómez [b], Gladis J. Labrada-Delgado [c], Salvador Fernández-Tavizón [b], Pedro J. Herrera-Franco [d], Srinivas Godavarthi [e], José G. Torres-Torres [a], Adrián Cervantes-Uribe [a], Claudia G. Espinosa-González [e],*

[a] *División Académica de Ciencias Básicas, Universidad Juárez Autónoma de Tabasco, Km. 1 Carretera Cunduacán-Jalpa de Méndez, La Esmeralda, C. P. 86690, Cunduacán Tabasco, México*
[b] *Laboratorio Nacional de Materiales Grafénicos, Centro de Investigación en Química Aplicada, Enrique Reyna Hermosillo 140, San José de los Cerritos, C.P. 25294, Saltillo Coahuila, México*
[c] *Laboratorio Nacional de Investigaciones en Nanociencia y Nanotecnología, Instituto Potosino de Investigación Científica y Tecnológica A.C, Camino a la Presa de San José 2055, Lomas 4ta, C.P. 78216 San Luis Potosí, S.L.P., México*
[d] *División de Materiales Avanzados, Centro de Investigación Científica de Yucatán, Calle 43 No. 130 por 32 y 34, Chuburná de Hidalgo, C.P. 97205, Mérida Yucatán, México*
[e] *Investigadoras e Investigadores por México-División Académica de Ciencia Básicas-Universidad Juárez Autónoma de Tabasco, Km. 1 Carretera Cunduacán-Jalpa de Méndez, La Esmeralda, C. P. 86690, Cunduacán Tabasco, México*

ARTICLE INFO

ABSTRACT

New ternary materials TiO$_2$-Al$_2$O$_3$-GnPs (TAG) were prepared by using an innocuous sol-gel method with a slight modification for the addition of graphene nanoplatelets (GnPs), under room temperature and atmospheric pressure. The materials TiO$_2$-Al$_2$O$_3$-GnPs were prepared with variations of concentration between 0.05 and 1 wt % of GnPs. In this study, we analyzed the physicochemical properties by X-ray diffraction (XRD) and UV-Vis spectroscopy, textural properties by N$_2$ physisorption, morphology by scanning and transmission electron microscopy (SEM, TEM) and a chemical species analysis was carried out by X-ray photoelectron spectroscopic (XPS). The photocatalytic activity of each material was evaluated in the degradation of a model molecule, Diuron, a carcinogenic and cytotoxic herbicide used in farm fields. To determine reaction selectivity and mineralization degree, the photocatalytic reaction was monitored by using UV-Vis spectroscopy and total organic carbon (TOC). In samples with higher GnPs' concentration, a good enough specific surface area of up to 379 m^2/g was observed, and reduced band gap energy (2.8 eV) with respect to TiO$_2$ and mixed oxide (3.2 and 3.1 eV respectively), was obtained. These resulting properties were the key indicator so that the materials could be applied as photocatalysts. In the photocatalytic activity determination, TAG-0.75 was the sample that showed the best results with respect to the mixed oxide; the highest photocatalytic conversion, the reduced average life time, and increased mineralization and reaction selectivity.

1. Introduction

In recent decades, pollution has also increased significantly worldwide with population growth. Therefore, science is busily working to develop new technologies and to provide solving alternatives for this problem [1,2]. One of the current alternatives is the design of nanomaterials with a photocatalytic application for pollutant degradation, hydrogen production and biofuel, and energy storage. To produce cheaper nanomaterials, with a convenient cost-efficiency relationship, is desired [3,4]. Efforts made from the area of materials are focused to develop efficient nanocatalysts for the remediation of water and soil. There is a lot of dedication to the study of graphene materials such as graphite, graphene, graphene oxide (GO), multi wall carbon nanotubes (MWCNT), etc., that have already been used to prepare composite materials with photocatalytic properties [5,6].

Particularly, graphene nanoplatelets (GnPs), due to their noteworthy intrinsic properties such as electrical conductivity of 1460

S/m [7,8,9] and specific surface area between 150 and 750 m^2/g [10] have gained relevance when manufacturing composites. GnPs are a mixed material constituted of single graphene sheets, a few piled up graphene layers, and graphite; they are produced by liquid phase exfoliation from graphite, a versatile method and the best for scaling up to massive production of defect-free monolayer graphene [11], which made them commercially available at low cost. GnPs also have minimal amount of oxidized groups that have allowed them to combine with other materials and offer a better cost-efficiency relationship compared to other graphene materials such as carbon black or carbon nanotubes [12]. However in most of the reported works, the GnPs produced on long scale have been studied as polymer matrix strengthener, in the design of hierarchical interface of epoxy composites, as anticorrosion coatings, and in the formulation of polymer and composite materials for energy generation and storage [13].The application of these GnPs prepared on a large scale, as an important component of a photocatalytic material used in the degradation of pollutants from water, has not been reported to the best of our knowledge.

On the other hand, the use of GnPs obtained on lab scale has been reported in the biomedical area to create biosensors for the cortisone control [14], as an additive for manufacturing nanolubricants [15], in applications as supercapacitor electrodes [16], in electronic components as sensors [17], and in the manufacturing of conductive polymers [13]. Not many but interesting works have been disclosed, where these GnPs are combined with different materials and it can greatly boost the photocatalytic activity towards the photo-destruction of contaminants such as heavy metals, dyes, pharmaceutics, antibiotics, phenols, polycyclic aromatic hydrocarbons, from the wastewater [18]. Among the reported are those based on zinc oxide ZnO [19,20,21], TiO_2 [22] and ferromagnetic oxides (of Co, Zn, Ca, Mg) [23,24,25,26]. Such materials have been obtained through complicated methods as co-precipitation, sintering in plasma, hydrothermal and solvothermal synthesis. Generally, the preparations have required considerable amount of GnPs according to the synthesis method, but the highest efficiency results have been obtained in materials that contain the lowest GnPs weight content. For example, Israr *et al.*, in 2021 [23] reported a 99.4% degradation efficiency for methylene blue under visible light by the use of a calcium-ferrite containing 0.25 wt % of GnPs.

And for what interests us, work is underway on the design photocatalysts based on GnPs to reduce herbicides environmental contamination. Diuron has been studied in depth since it is considered highly toxic, cytotoxic, and carcinogenic [27] with a persistent half-life of more than 300 days [28]. Diuron characteristics make it a suitable model molecule for testing new materials with photocatalytic applications. Hence in this investigation, the photocatalytic activity of the ternary material TiO_2-Al_2O_3-GnPs synthesized by the simplest sol-gel method was evaluated due to the interest for exploring it in the degradation of an herbicide (Diuron) under UV-Vis radiation. We recognize that the promise of GnPs produced on long scale, of contributing with their high electrical conductivity and high specific area in this type of applications, motivated us to explore the performance of a new material that has not been disclosed and here is detailed.

2. Materials and methods

2.1. Synthesis of TiO_2-Al_2O_3-GnPs

All reagents (titanium butoxide, aluminum tri-sec-butoxide) and solvents (ethanol, butanol) were supplied from Sigma Aldrich and used as received. GnPs (GnP-750 grade C) as powder was provided by XG Sciences In., and exfoliated prior to use.

Sol-gel synthesis of TiO_2-Al_2O_3-GnPs was conducted in a three neck reactor by blending titanium butoxide (Sigma-Aldrich, (Ti ($OC_4H_9)_4$, 97%)) and aluminum tri-sec-butoxide (Sigma-Aldrich (Al [$OCH(CH_3)C_2H_5]_3$, 97%) at 60°C dissolved in 1-Butanol (ACS reagent, ≥99.4%) and 2-Butanol (ReagentPlus, ≥99%) respectively. GnP was exfoliated in a 1:1(v:v) mixture of water and ethanol (Sigma-Aldrich (CH_3CH_2OH 95%)) by 45 min treatment in an ultrasonic bath. The GnPs suspension containing from 0.05 to 1 wt% was dropped slowly into the reaction mixture under stirring and reflux and kept under those conditions during 24 h. The solvents were then removed under vacuum through the use of a rotoevaporator and the resultant material was dried at 120°C for 12 h and calcined at 500°C for 4 h using a ramp of 2°C/min. The materials obtained were labeled as TAG- followed by the percentage by weight of GnPs and pure materials as Ti for TiO_2, Al for Al_2O_3, TiAl for TiO_2-Al_2O_3 and GnPs for graphene nanoplatelets.

2.2. Equipment

Crystalline structures of the pure materials Ti, and Al, mixed oxide TiAl and the ternary composites with GnPs (TiO_2-Al_2O_3-GnPs) were determined using powder X-ray diffraction (XRD) on a BRUKER diffractometer equipped with a Cu Kα X-ray source and detector Linxeye (0.02°/3 s). The catalysts' optical characteristics were determined using a power spectrophotometer (Varian Model Cary III) by absorbance and the TAUC band gap was calculated. Surface area, pore size and volume were determined using BET method from N_2 adsorption-desorption isotherms which were recorded using an analyzer Micromeritics TriStar II, at -196°C; previously, samples were degassed at 300°C for 2 h purging with nitrogen gas. The samples' morphology and composition were analyzed using a field emission scanning electron microscopes FEI QUANTA FEG-250 and a FEI dual beam Helios Nanolab 600. Samples were placed on carbon tape and coated with gold; also, they were inspected by transmission electron microscopes with a FEI-QUANTA field emission TEM at 200-300 kV using sample dropdeposit on a copper grid. A K-Alpha X-ray photoelectron spectrometer (XPS) from Thermo Scientific Fischer, with Al Ka monochromatic radiation and energy resolution of 0.1 eV, was employed for oxidation states determination and elemental abundance analysis. For the photocatalytic evaluation, a UV photoreactor was used, equipped with a UV lamp of 13 W and wavelength at 365 nm.

2.3. Photocatalytic activity measurements

Photocatalytic activity of the materials was evaluated in a photoreactor by decomposition of a 30 ppm Diuron solution, a catalyst concentration of 0.4 g /L was employed. The solution was magnetically stirred during 30 min under darkness to ensure the Diuron adsorption/desorption equilibrium on the catalyst's surface. 6 mL of the suspension was collected at 15, 30, 45, 60, 120, 180 and 240 min. Diuron degradation was monitored by UV-Vis spectroscopy (Varian Cary III) and by total organic carbon content using a Shimadzu TOC-l plus TNM-l instrument.

3. Results and discussion

3.1. Structural analysis

The crystalline structure was studied by XRD analysis, the X-ray powder diffractograms of reference and ternary materials are shown in Figure 1. The Ti sample presented diffraction signals at 2θ: 25.2°, 37.7° and 48° [29,30] which are associated with the anatase phase of titanium oxide. The Al sample presents characteristic diffraction signals at 2θ: 37.6°, 45.8°, 66.8° of the γ-Al_2O_3 structure [31,32]. These signals were confirmed according to JCPDS 29-0063 and JCPDS 21-1272 cards. A crystalline structure was not

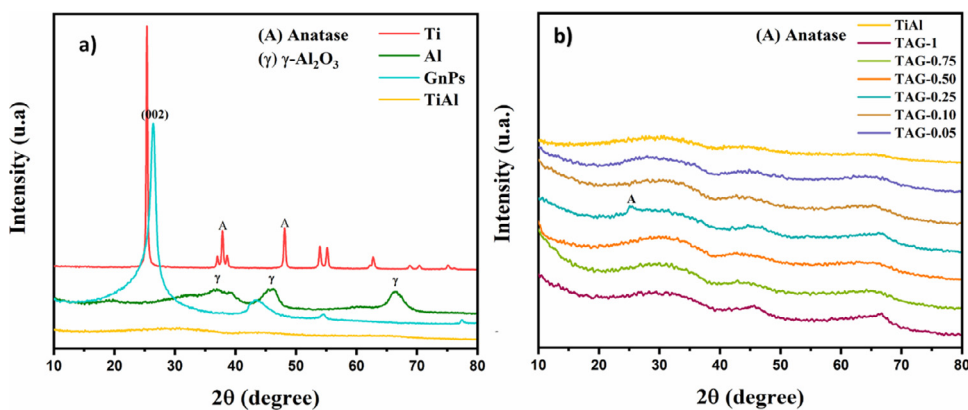**Fig. 1.** XRD diffractograms of (a) Ti, Al, TiAl and GnPs samples; (b) TiAl reference and TAG (TiO_2-Al_2O_3-GnPs) samples with 1.0 -0.05 wt% of GnPs.
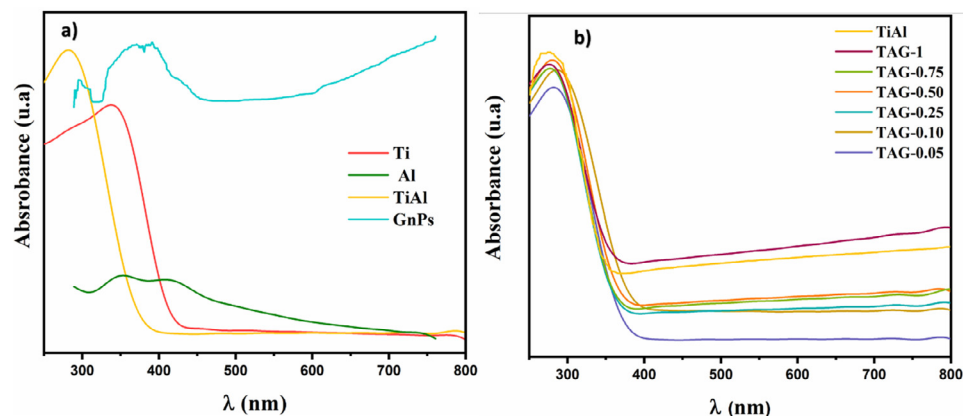

Fig. 2. UV-Vis spectra of a) Ti, Al, TiAl and GnPs samples and b) TAG (TiO_2-Al_2O_3-GnPs) samples with 1.0-0.05 wt% of GnPs.

observed for TiAl sample, in its stead, widened signals were observed, suggesting that the material has a disordered or amorphous structure. The diffractogram obtained from the GnPs shows the characteristic peak of graphene material at 2θ: 26.2° that corresponds to the crystalline plane (002), this was confirmed with the JCPDS 75-1621 card. In addition, others diffraction signals of lower intensity are observed and are also characteristic of standard graphitic carbon at 2θ: 42.2°, 44.3° and 53.9° corresponding to the crystalline planes (100), (101) and (004) respectively [33].

Most ternary materials showed diffractograms with undefined signals, indicating unordered structures (see Figure 1b) similarly to that of TiAl in Figure 1a. By exception, a probable anatase signal was detected at 25.2° 2θ in the TAG- 0.25 sample. The appearance of this TiO_2 phase could be explained by the fact that the GnPs favours the formation of the anatase phase in the material. Furthermore, in the TAG-1 sample, low intensity signals corresponding to the crystalline structure of γ-Al_2O_3 are detected at 2θ: 45.8°, 66.8°. In the same way, the presence of this phase could be due to a stabilizing effect of the GnPs' higher concentration on the γ-alumina phase. Despite the above, differences among the diffractograms of the TAG materials were not significantly apparent, and could be irrelevant and independent of the GnPs' content.

3.2. Optical properties

UV-Vis absorption spectra of the reference materials are shown in Figure 2a, it can be seen that the absorption starts at 406 nm, suggesting a weak absorption in the visible region; mixed oxide TiAl experienced absorption towards the UV region at 367 nm and a higher absorption respect of Ti (pure titanium). The Al material shows the lowest absorbance between 310 nm and 725 nm, while

Table 1
Textural properties and band gap energy (*Eg*) of samples

Samples	*Eg* (eV)	S_{BET} (m^2/g)	V_{BJH} (cm^3/g)	Pore average diameter (nm)
Ti	3.2	62.85	0.19	10.20
Al	–	239.68	0.92	10.61
GnPs	–	581.80	0.75	7.47
TiAl	3.1	388.30	0.65	6.85
TAG-1	2.9	339.83	0.76	5.85
TAG-0.75	2.8	379.33	0.76	5.48
TAG-0.50	3.0	325.92	0.51	4.31
TAG-0.25	3.0	295.33	0.63	6.87
TAG-0.10	3.0	319.39	0.54	4.47
TAG-0.05	2.9	236.00	0.36	4.17

GnPs, being a dark-bodied material, tend to absorb across the entire spectrum. Figure 2b presents the spectra of the TAG samples (TiO_2-Al_2O_3-GnPs), clearly showing absorption in the UV region, with the maximum absorption slightly shifted towards the visible region as compared with the TiAl reference. An increases in absorbance was not observed, and absorption edges present in the violet region. A minimal relationship of optical characteristics with respect to GnPs content was expected, however, the changes were rather random and are probably due to others factors such as the GnPs distribution and/or the nature of the interactions with the mixed oxide.

The band gap energy (*Eg*) of the material was estimated from the UV-Vis absorption spectra by means of TAUC model and the results are shown in Table 1. It can be observed that when comparing the values of TiAl mixed oxide *Eg* (3.1 eV) to those of the TAG materials (2.8-3.0 eV), the band gap is narrower. The results
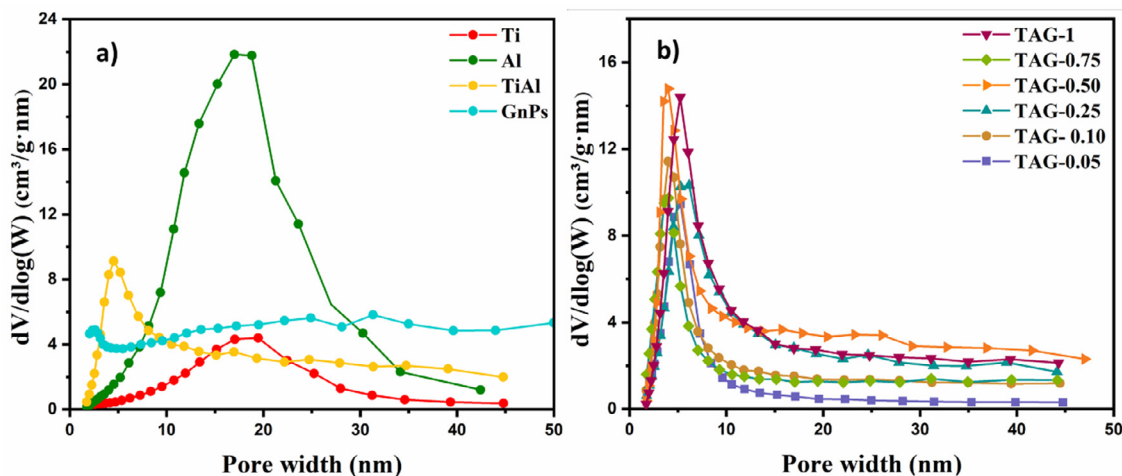
Fig. 3. Pore size distribution from N_2 adsorption/desorption analysis of a) Ti, Al, TiAl, and GnPs samples, and b) TAG (TiO$_2$-Al$_2$O$_3$-GnPs) samples with 1.0-0.05 wt% of GnPs.

indicate that TAG-0.75 has the lowest band gap value at 2.8 eV, however, no marked effect was observed by varying the sample's GnPs content.

3.3. Textural properties

Isotherms of N_2 adsorption/desorption for the reference materials and TAG samples are presented in Figure S1. The textural analysis indicated that the Al, Ti, and TiAl materials exhibited a type IV isotherm which is characteristic of mesoporous materials with a pore diameter of 2 nm to 50 nm [34]. GnPs and TiAl exhibit H3 hysteresis cycles, that of the GnPs is characteristic of plate-like materials, while that of the TiAl corresponds to an unfilled pore network [35]. All TAG samples exhibited IV type isotherms and H2 and H3 hysteresis cycles. Specific surface area, pore average size, and pore volume of all samples are listed in the Table 1.

In case of TAG materials, when compared with there were specific surface area values equivalent to those of the TiAl samples. The maximum value at 379.3 m^2/g was observed for the TAG-0.75 sample; the lowest value at 236 m^2/g was shown by the TAG-0.05 sample, what corresponds to a decrease of ∼ 39% when compared with the specific surface area of the TiAl reference; the smallest pore volume value at 0.36 cm^3/g was also observed in this sample. This effect could occur according to two possible scenarios that in Figure S2 can be seen: the first in which graphene single-sheet and platelets of few graphene single-sheets, are obstructing the pores and/or closing the interstices among the particles of the material; the second scenario where the lowest load of GnPs simply gave rise to a more compacted material. The decrease in specific surface area and pore volume could be explained by the strain in the amorphous-like structure of TiO$_2$-Al$_2$O$_3$ [36], where the geometry of the crystals is modified by the GnPs, thus favoring more stable structures such as that of anatase which also was barely observed by XRD.

For a better understanding of the material characteristics, the main populations of pore size were analyzed. The pore size distributions for the reference and ternary materials are shown in Figure 3. The Ti sample in Figure 3a) showed a Gaussian distribution corresponding to a predominant population of mesopores of ∼18 nm. Comparatively, Al sample showed a broader pore size distribution than that of Ti, with two prevailing pore sizes within the mesopores range, between 18 nm and 20 nm. TiAl sample presented a unimodal distribution of pore size centered at 4.8 nm. In the case of the GnPs sample, the pore size is extended throughout the meso and microporous regions, indicating that these agglomer-

ated nanoplatelets with nanopores, constitute a microporous material.

The addition of GnPs into the TiAl during the synthesis, produced materials with unimodal distributions of pore size centered between 4 and 6 nm (see Figure 3b); these values, although they are lower than those of pure Ti and Al, are equivalent to those of TiAl, and could be explained by the fact that graphene single-sheet and few-layer graphene nanoplatelets are not affecting to the morphology and porosity of TiAl.

3.4. Morphology analysis

To investigate the effect of GnPs on the morphology of ternary materials, these were inspected by field emission scanning electron microscopes (FE-SEM) and transmission electron microscopy (TEM).

Initially, the reference materials were surveyed and Figure 4 shows SEM images of Ti, Al, TiAl, and GnPs; Figure 4a) corresponds to Ti sample, which shows semispherical TiO$_2$ particles of 1.6 to 3.6 μm diameter, typically indicative of the anatase phase [37].

The Al sample, Figure 4c) image, presents a grouping of overlapping irregular plates. Figure 4d) shows GnPs sample with a characteristic morphology of agglomerates of nanometric sized platelets. Morphology of the TiAl material is distinguished from that of pure materials by being flaky with irregular shapes and edges, and random distribution, shown in Figure 4b).

The resulting morphology after the synthesis of TAG samples, is shown in Figure 5. The morphology observed in the mixed oxide, persists in the ternary materials as flakes from clustered particles and with irregular edges. In the Figures 5a), 5b), and 5c), corresponding to the TAG samples containing 1.0, 0.75, and 0.50 wt% of GnPs respectively, it can be seen that GnPs are dispersed and appear to be surrounded or covered by mixed oxide. For these samples, GnPs can be localized with relative facility because they are present in higher proportions. In the Figures 5d), 5e), and 5f) corresponding to the TAG-0.25 sample, it can be seen as the flakes of ternary material are formed from accumulated grains. On the other hand, smooth sheets of GnPs cannot be seen in this sample, due to the low proportion of GnPs present. Nevertheless, and despite the lowest GnPs load, in the Figure 5i) of TAG-0.05 sample, it is possible to observe (circled zone) that clustered material grew on the smooth sheets of GnPs, like grains.

To further investigate the synthetized material morphology, TEM images were acquired. The reference materials are shown in Figure 6; the image in Figure 6a) corresponds to the Al sample, it
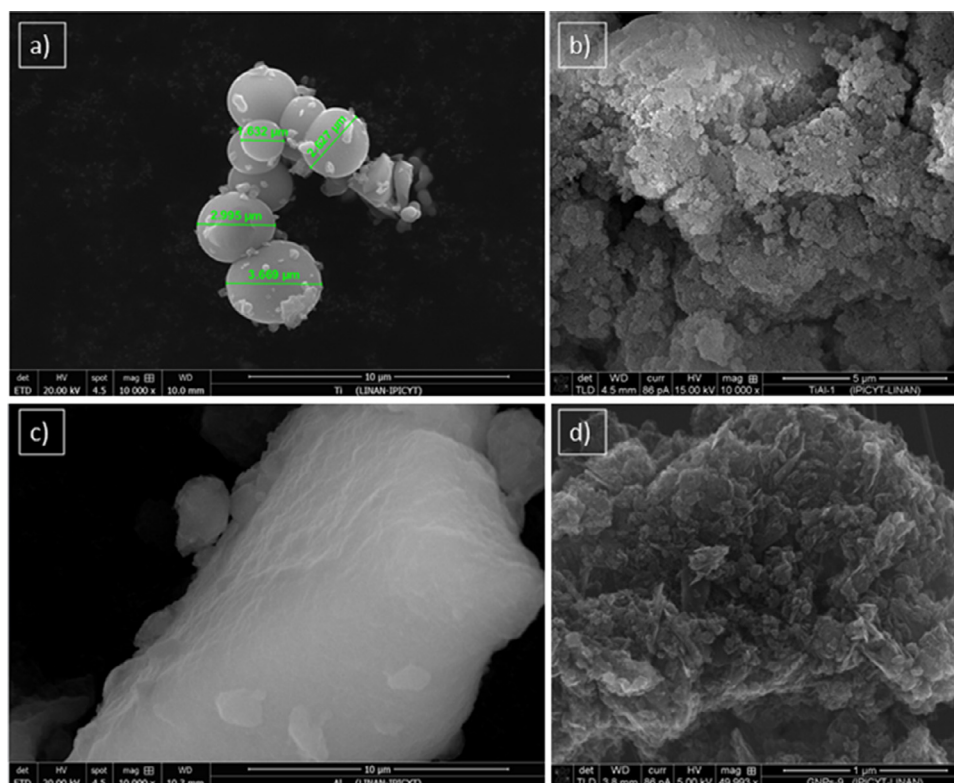
Fig. 4. SEM images of reference materials, in a) Ti, b) TiAl, c) Al, and d) GnPs.

can be observed that there are particles like needles or wires, it is also appreciable that the material is constituted with other abundant particles as irregular plates; this morphology is typical of γ-alumina according to reported [38]. The image in Figure 6b) corresponds to that of the Ti sample, showing a cluster formed from semi-spherical particles of different densities, with some particles showing their hollow interior. It has been reported that anatase phase TiO_2 powders, consist of particles with spherical morphology [39,40] as can be appreciated from the SEM and TEM microphotographies.

As seen in Figure 6c)-6i) of the TiAl sample, the alumina wire-morphology is maintained in the composite, together with a different and apparently amorphous phase; it is worth noting that the semi spherical morphology associated with TiO_2 cannot be found. The circled zone in Figure 6d) was magnified and presented in Figure 6e) showing wire structures 3-5 nm wide and few ten nanometers in length. Figure 6f) and 6g), show dense and thinner particles, constituted of amorphous material, small wire particles and plates with irregular edges; however amorphous particles devoid of wires or plates can be seen in Figure 6h) and Figure 6i), indicating the sample's amorphous nature.

TEM images of TAG samples are shown in Figure 7. All samples exhibit the same morphology than that of the TiAl reference compound, i.e., the alumina wire-morphology and the amorphous particles of TiO_2 devoid of wires in Figure 7a) and Figure 7c) respectively, can be observed. In Figures 7d) to 7f) is possible to discern the presence of GnPs sheets embedded in the mixed oxide materials. It is important to highlight that no changes in the oxides' morphology can be observed with varying GnPs concentration.

3.5. TAG samples' XPS analysis

Oxidation states determination was carried out by XPS analysis and a survey scan corresponding to TAG-0.75 sample is presented in Figure S3; the analysis of this sample is relevant because

Table 2
Species abundance from high resolution XPS spectra of TAG-0.75 sample.

Peak	Atomic abundance (%)	Species	Species abundance (%)
Ti 2p	8.72	Ti^{4+} (Ti−O)	45.06
			31.20
		Ti^{3+} (TiOx),	6.49
		O-Ti=O-C	17.25
Al 2p	23.4	Al−O	90.3
		Al−OH	9.68
O 1s	53.2	M−O (M= Al ,Ti)	75.34
		HO⁻	24.66
C 1s	14.6	C=C	56.57
		C−C	23.13
		C=O	14.41
		O−C=O	5.90

it presented an outstanding behavior in the photodegradation application, which will be discussed later. Wide survey spectrum confirmed the presence of the sample's principal elements, Deconvoluted high-resolution spectra of Ti 2p, Al 2p, O 1s, and C 1s atoms are shown in Figure 8. Peaks Ti 2p3/2 and Ti 2p1/2 were obtained from the Ti 2p spectrum, presented in Figure 8a) and located at 458.9 eV and 464.6 eV respectively [41]. They are attributed to Ti^{4+} species of Ti−O bonds formed in a −Al−O−Ti≡ amorphous-like structure of the Al_2O_3−TiO_2 [22]. Species abundance from high resolution XPS spectra of TAG-0.75 sample are shown in Table 2.

Two little peaks at 457.6 eV and 460.5 eV are observed and to Ti^{3+} species as TiOx (x=1-2) were assigned; such species are found when interactions between the metal oxide and the GnPs are formed [42]. Theoretical and experimental studies have found that metals and metal oxides form interactions that allow them to grow from the graphene sheet edges if these contain dangling −OH groups. Graphene sheets can also nucleate or facilitate the growth by chemisorption of metal oxide particles by local strain due to C−
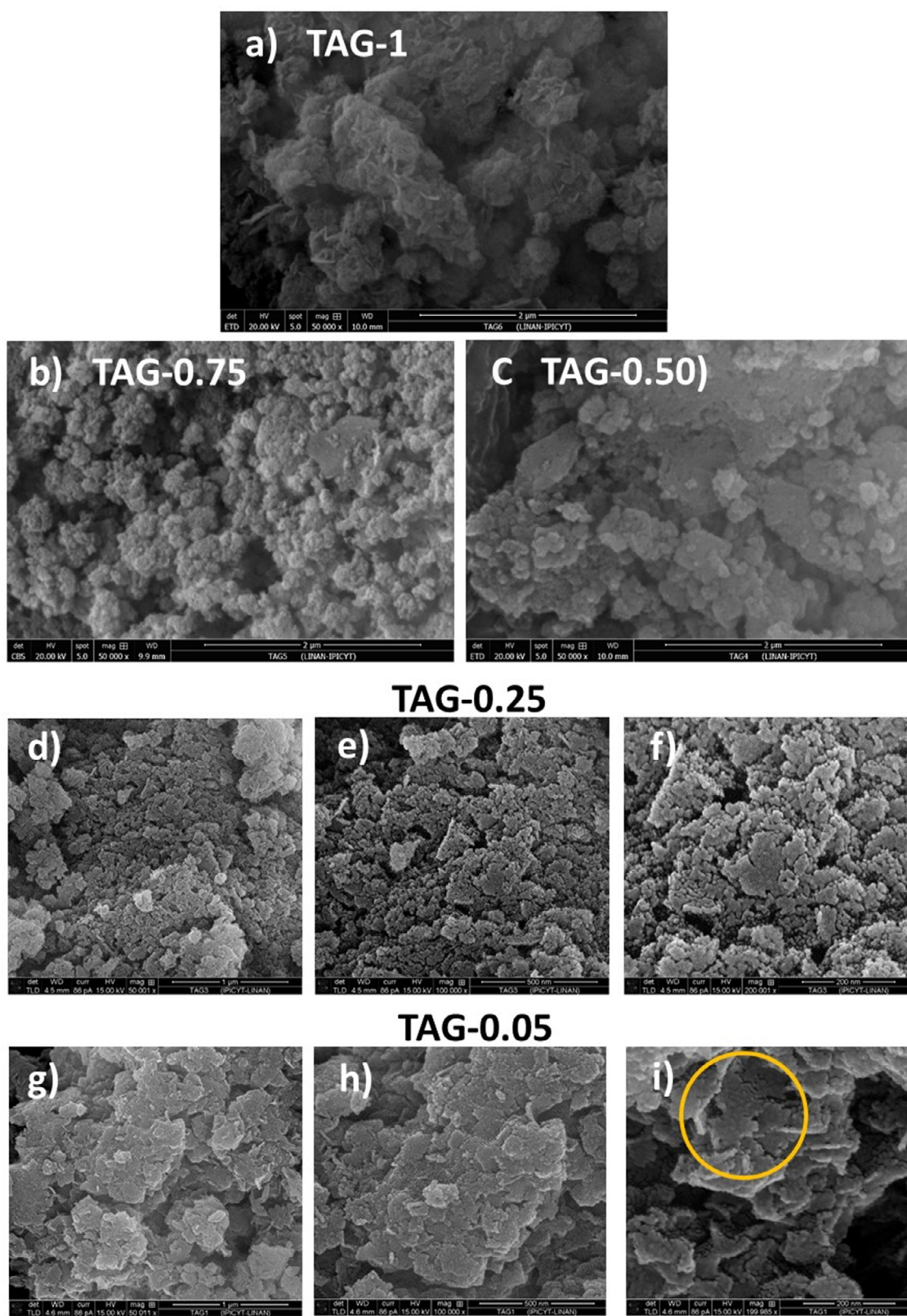
A.d.J. Zurita-Yduarte, D.J. Gallegos-Hernández, U.A. Sierra-Gómez et al.

Carbon Trends 9 (2022) 100213

Fig. 5. SEM images of a) TAG-1; b) TAG-0.75; c) TAG-0.50; d)-f) TAG-0.25 scale bar at 1μ, 500 nm and 200 nm respectively; g)- i) TAG-0.05 scale bar at 1μ, 500 nm, and 200 nm respectively.
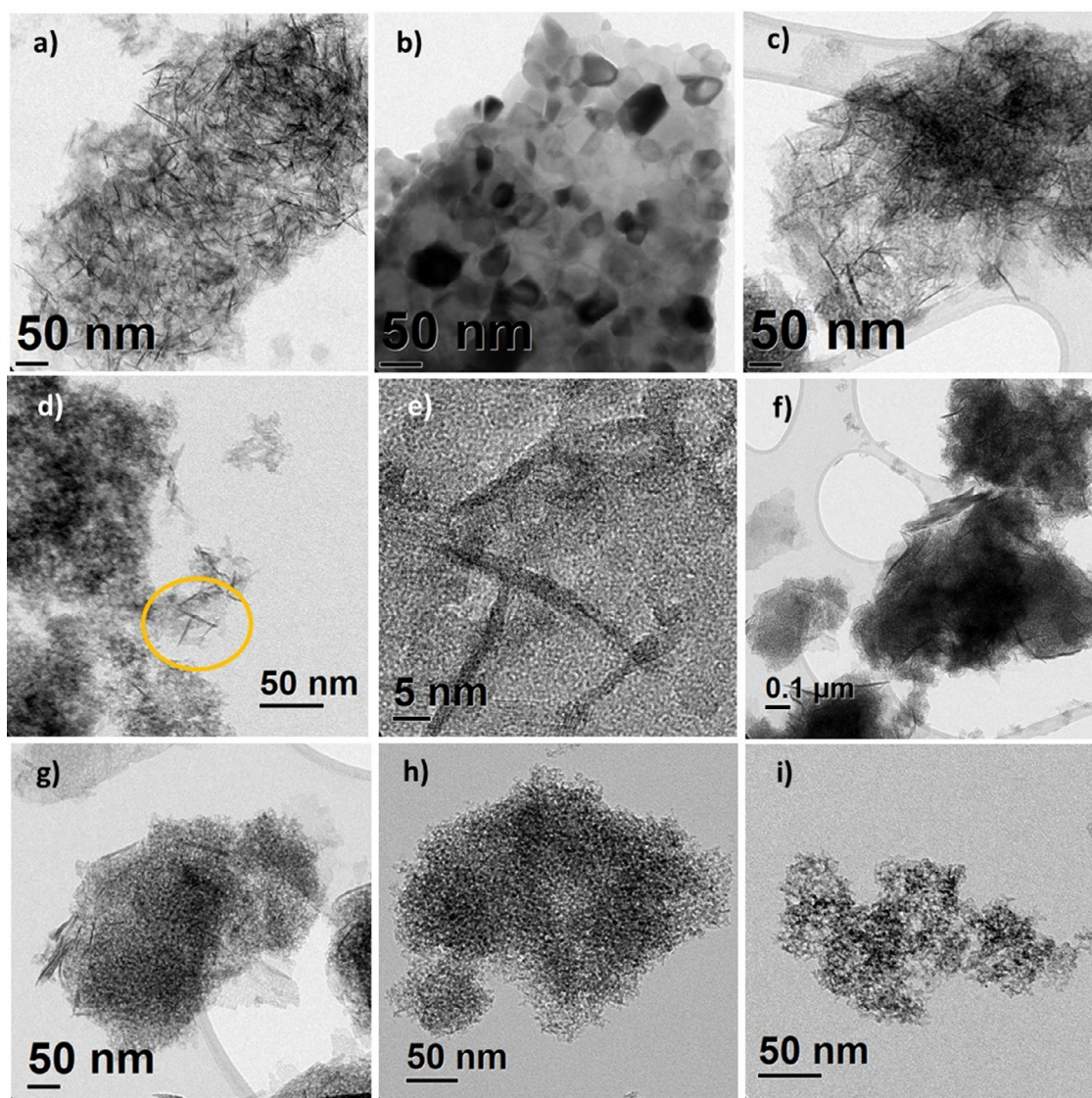
Fig. 6. TEM images of the reference materials at different magnifications, in a) Al, b) Ti, and c)-i) TiAl.

C binding in graphene lattice, or by interaction with high-energy defect sites such as pentagon-hexagon pairs or vacancies present in the graphene lattice [43,44]. Recently, M. F. Mazza et al., [45] deposited TiO_2 and Al_2O_3 films onto graphene monolayer by taking advantage of the reactivity differences between defect regions and inert basal plane regions in graphene sheet. As the authors did not previously oxidized the graphene sheets, the deposition took just on the sheet's defect sites. Consistently, Al_2O_3 resulted in an isotropic film deposited onto graphene monolayer while the TiO_2 nucleated at the boundaries.

Since in our work no acid was used in the sol-gel process, the nanoplatelet basal plane was not saturated with water molecules or hydroxyl groups. Thus, reactive sites should be in graphene layer defects of the GnPs. Therefore, the new chemical interactions as $O-Ti=O-C$ binding was formed at those defect sites, allowing the nucleation and growth of mixed oxide, as can be seen in the SEM images of Figure 5. In addition, it is known that the Ti^{3+} valence state of TiOx species changes the electronic band structure of TiO_2 [46], creating a new energy level in the band gap, and consequently contributing to its reduction [47]. We suggest that the $-O-Ti=O-C$ binding associated to Ti^{3+} species, decreases the band gap observed in our case.

The Al 2p peak in Figure 8c) was obtained from deconvoluted spectrum, it shows binding energies at 74.3 eV and 75.6 eV corresponding to Al^{3+} species of $Al-O$ and $Al-OH$ binding respectively [29,48]. Deconvoluted high-resolution spectrum for O 1s, is shown in Figure 8b), the signal at 530.7 eV is characteristics of O^{2-} species corresponding to $M-O$ binding as of $Ti-O$ and $Al-O$ [29]. The peak at 532.4 eV can be assigned to HO^- species adsorbed onto material surface [46]. A deconvoluted spectrum for C 1s element was also obtained and presented in Figure 8d), the peak at 284.3 eV is in agreement with $C=C$ binding of graphitic planes. A peak at 285 eV was assigned to $C-C$ binding in GnPs; also a peak at 286.1 eV is in agreement with the $C-OH$ hanging species from the GnPs edges. In addition, peaks at 287.5 eV, and 289.9 eV agree well with $C=O$ and $-O-C=O$ bonds of carbonyl and carboxyl groups, respectively [49,50] which are expected to be present at the GnPs' functionalized edges.

3.6. Photocatalytic activity of TiO_2-Al_2O_3-GnPs

Photocatalytic performance of all synthetized samples was evaluated in the degradation of Diuron under UV light irradiation. Figure 9 shows the results from data obtained, degradation development was determined using Eq. 1 [51], results are listed in
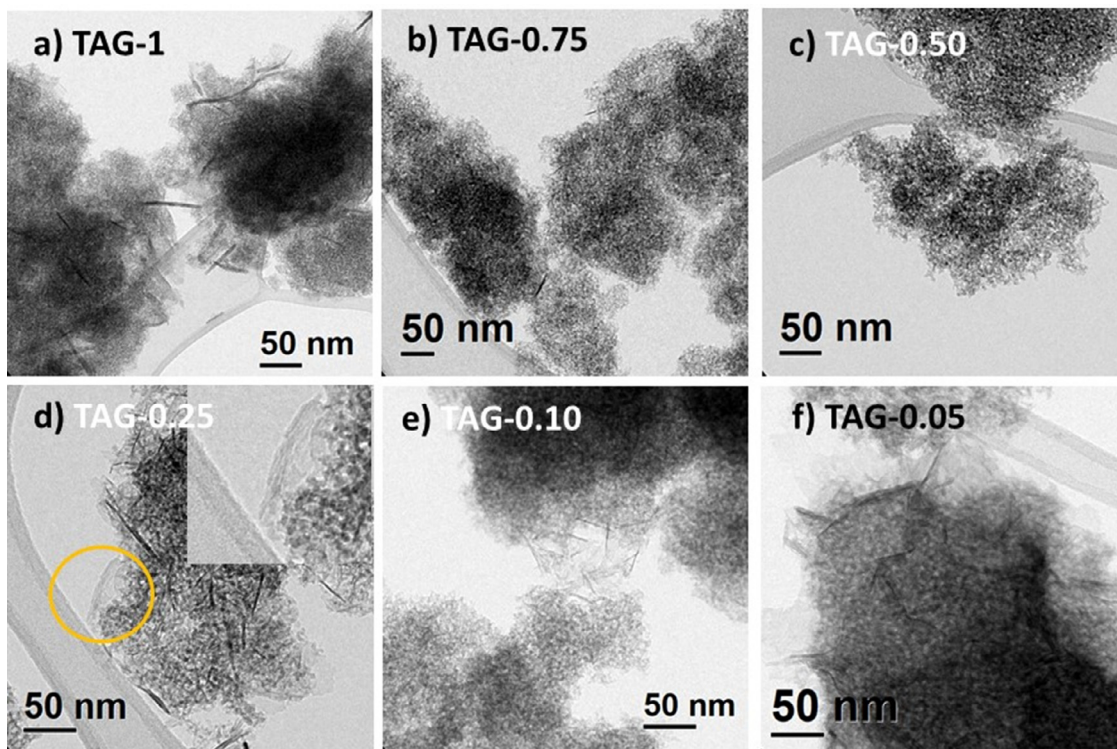
Fig. 7. TEM images of the synthesized ternary materials TAG (TiO$_2$-Al$_2$O$_3$-GnPs) samples with 1.0-0.05 wt% of GnPs.
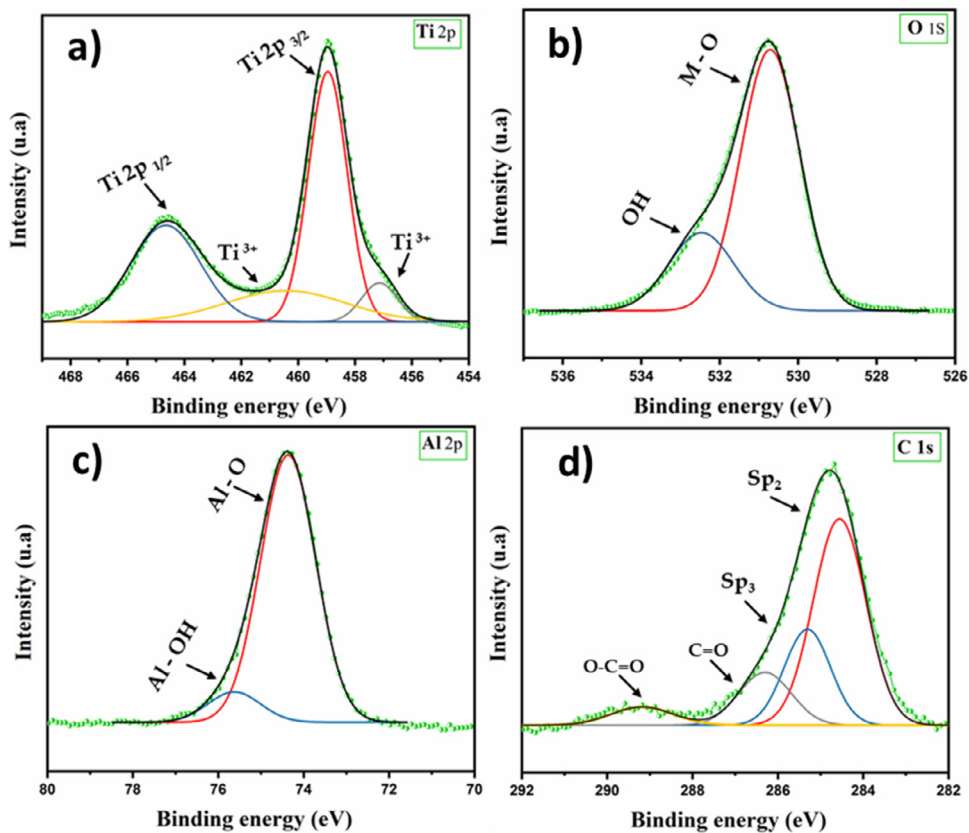

Fig. 8. High resolution XPS spectra from the TAG-0.75 sample, in a) Ti 2p, b) O 1s, c) Al 2p, and d) C 1s elements.
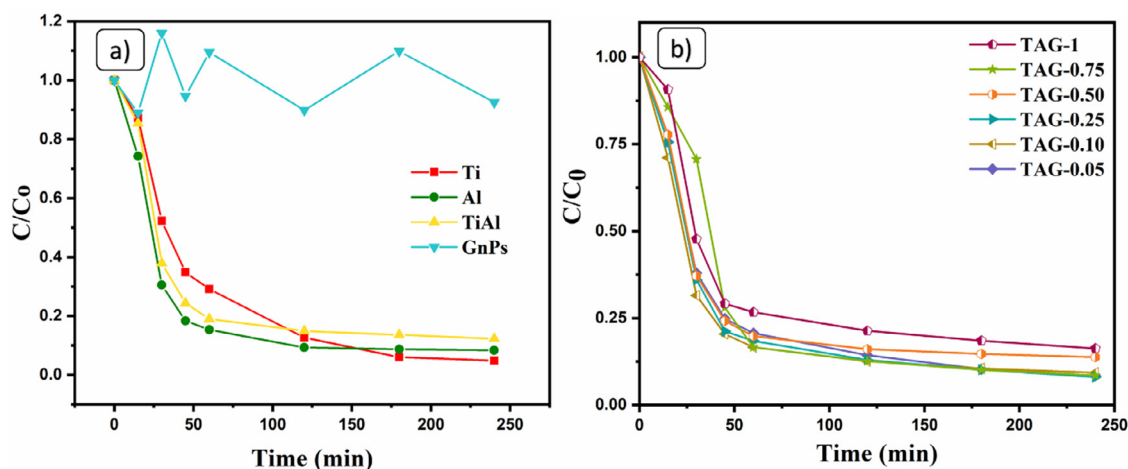
Fig. 9. Photodegradation of Diuron using as catalyst: a) Ti, Al, TiAl and GnPs, b) TAG (TiO_2-Al_2O_3-GnPs) samples with 1.0-0.05 wt% of GnPs.

Table 3
Photodegradation of Diuron under catalytic conditions.

Material	Degradation (%)*	K (min^{-1})**	$t_{1/2}$ (min)	TOC (%)*	S_{CO2} (%)
Ti	95.0	0.022	30.73	22.0	23
Al	91.6	0.034	20.23	15.2	16
GnPs	7.40	0.001	427.86	27.3	–
TiAl	87.7	0.030	22.73	20.5	23
TAG-1	83.7	0.025	27.52	34.0	40
TAG-0.75	91.5	0.031	22.09	45.7	49
TAG-0.50	86.2	0.029	23.61	35.0	40
TAG-0.25	92.0	0.031	22.34	26.0	28
TAG-0.10	90.7	0.032	21.50	28.0	30
TAG-0.05	91.6	0.028	24.35	24.4	26

* 240 minutes
** 60 minutes.

Table 3.

$$\% \, Degradation = \left(1 - \frac{C}{Co}\right) x \, 100 \qquad (1)$$

The amount of degraded molecules in the Diuron solution, was determined by total organic carbon (TOC) at the reaction final time, and in order to know how much organic molecules were converted to CO_2, the selectivity was calculated as well.

It can be observed in Figure 9a) that for Ti, Al, and TiAl, the maximal molecular degradation occurred in the first 60 min of irradiation therefore, the kinetic constant k (degradation reaction velocity) was calculated at 60 min of reaction. It is important to note that, according to degradation evolution, the reaction can be well approximated as pseudo-first-order kinetic during this tame. Ti sample was expected to show the largest photocatalytic response under ultraviolet light and therefore, the highest degradation (95%) due to its band gap at 3.2 eV and to its high absorption capacity however, TiAl sample shown significant values of degradation (87.7 %) and k (0.030 min^{-1}) and for this reason we used these results as reference values.

Except for the samples TAG-1 and TAG-0.50, most synthetized materials presented higher degradative capacity between 91.5% and 92.0 % respect to TiAl (87.7%), Figure 9b). Although TAG-1 presented the lowest degradation levels, it presented moderately improved levels of mineralization and selectivity w.r.t. TiAl; this result can be explained by the fact that GnPs load is such that the sample is saturated, and possibly agglomerated nanoplatelets produce poor performance [52,53]. The best performance was observed in the TAG-0.75 sample with degradation level of 91.5%, mineralization of 45.7%, and 49% of selectivity; TAG-0.25 might be outperforming it slightly in degradative capacity with 92.0% but the mineralization and selectivity are among the lowest observed, 26% and

28% respectively; this discreet improvement in degradative capacity could be associated to the small proportion of anatase phase present in the sample (as observed by XRD characterization) however, this condition is not enough to achieve a minimum acceptable mineralization. All the above means that TAG-0.75 sample is the material that showed the most efficient degradation of the organic compounds and that the photocatalytic performance observed is the consequence of the material's lower band gap energy and its higher specific surface area [54]. Impossible not to mention the TAG-0.05 sample because its degradative capacity is not negligible but, k, mineralization, and selectivity, are at the same level that of the reference material, i.e., the GnPs concentration is a lot of small that its contribution is not clear.

In addition, we interpret from the photocatalysis results observed in TAG samples, that there is evidence of the important role that GnPs performances in the ternary material; the GnPs incorporation improved the photocatalytic performance up to a maximum point of GnPs load that when it is exceeded, the performance doesn't seem to improve (percolation), i.e., with the use of an exceeded GnPs load, photons could be quenched on the photocatalyst surface, and to produce a poor photocatalytic performance and causing the decrease in photodegradation efficiency as occurred in TAG-1 sample [55].

Our current results obviously suggest that the Diuron molecular degradation using TiO_2-Al_2O_3-GnPs nanocomposites occurred according to a photocatalytic reaction by means of radical species; a schematization of the photodegradation reaction is suggested in Figure 10.

The photocatalytic reaction starts with the light excitation of the TiO_2 semiconductor's electrons from the valence band to the conduction band; the electrons then are transferred to the GnPs
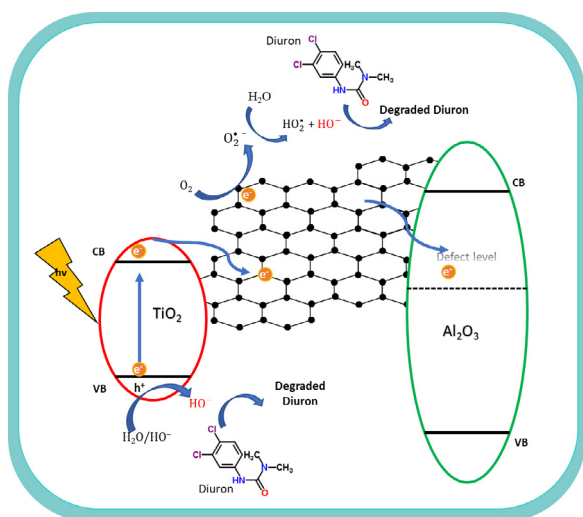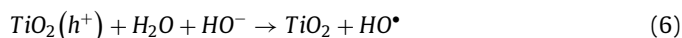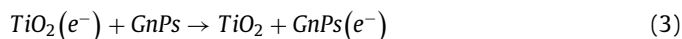
A.d.J. Zurita-Yduarte, D.J. Gallegos-Hernández, U.A. Sierra-Gómez et al.

Carbon Trends 9 (2022) 100213

Fig. 10. Schematization of the photocatalytic activity of compound Ti$_2$O-Al$_2$O$_3$-GnPs.

integrated within the ternary compound and finally transferred to the defects present in the alumina. This effective charge transfer through the GnPs reduces the recombination rate of e^-/h^+ pairs so that the electrons are ensnared in the alumina, completely avoiding the recombination thereby increasing the photocatalytic efficiency.

Photo-induced electrons tend to react with absorbed O$_2$ to generate the superoxide anion (O$_2^{\bullet -}$) species in the GnPs conduction band; while in the valence band of TiO$_2$, h^+ react with surface-bound H$_2$O and HO$^-$ species to produce hydroxyl radicals (HO$^{\bullet}$). The mechanism can be summarized by Eq. 2 to Eq. 6.

$$TiO_2 + h\nu \rightarrow TiO_2\left(e^- + h^+\right) \tag{2}$$

$$TiO_2\left(e^-\right) + GnPs \rightarrow TiO_2 + GnPs\left(e^-\right) \tag{3}$$

$$GnPs\left(e^-\right) + O_2 \rightarrow O_2^{\bullet -} + GnPs \tag{4}$$

$$O_2^{\bullet -} + H_2O \rightarrow HO_2^{\bullet} + HO^- \tag{5}$$

$$TiO_2\left(h^+\right) + H_2O + HO^- \rightarrow TiO_2 + HO^{\bullet} \tag{6}$$

Here, GnPs play an important role in the photocatalytic activity of TAG composites because as reported previously, the planar π-conjugated structure of GnPs makes it an excellent electron accepting material [56], generating a greater quantity of electrons available for the radical production.

4. Conclusions

Compounds of TiO$_2$-Al$_2$O$_3$-GnPs containing different concentrations of commercial and produced on long scale GnPs, have been prepared successfully by using sol-gel method and proved in the photodegradation of Diuron.

Characterization results suggest that the synthesis gave rise to a mesoporous ternary material, with decreased band gap energy, when the GnPs' concentration in the compound was 0.075 wt%. XRD analysis helped to confirm an amorphous-like structure in TiO$_2$-Al$_2$O$_3$-GnPs and XPS spectroscopy revealed that the compound is based on bonds –Al–O–Ti≡. Also, the presence of bonds

–O–Ti=O–C confirmed interfacial interactions between mixed oxide and GnPs. Such material with amorphous-like structure nucleated and grew on the GnPs basal plane according to observations by microscopy SEM and TEM.

Photocatalytic evolution experiments evidenced that when GnPs' concentration in the compound was of 0.075 wt%, the highest conversion of Diuron to CO$_2$ was obtained compared to the compounds with different GnPs' concentration; such activity occurred due to the decreased band gap and the highest specific surface area observed in TAG-0.75 sample.

Declaration of Competing Interest

The authors declare the following financial interests/personal relationships which may be considered as potential competing interests. Pedro J. Herrera-Franco reports equipment, drugs, or supplies was provided by XC SCIENCES In.

CRediT authorship contribution statement

Alina de J. Zurita-Yduarte: Investigation, Writing – original draft. **Diana J. Gallegos-Hernández:** Investigation. **Uriel A. Sierra-Gómez:** Investigation, Validation, Visualization, Writing – review & editing. **Gladis J. Labrada-Delgado:** Resources, Validation, Visualization, Writing – review & editing. **Salvador Fernández-Tavizón:** Writing – review & editing. **Pedro J. Herrera-Franco:** Resources. **Srinivas Godavarthi:** Visualization. **José G. Torres-Torres:** Resources. **Adrián Cervantes-Uribe:** Resources, Methodology, Supervision, Validation. **Claudia G. Espinosa-González:** Conceptualization, Supervision, Visualization, Resources, Writing – review & editing.

Acknowledgements

Supplementary materials

Supplementary material associated with this article can be found, in the online version, at doi:10.1016/j.cartre.2022.100213.

References

[1] J. Castilla-Archilla, V. O'Flaherty, P.N.L. Lens, Biorefineries: industrial innovation and tendencies, in: J.R. Bastidas-Oyanedel, J. Schmidt (Eds.), Biorefinery, Springer, Cham, 2019, pp. 3–5, doi:10.1007/978-3-030-10961-5_1.

[2] Y. Kumar, S. Rawal, B. Joshi, S.A. Hashmi, Background, fundamental understanding and progress in electrochemical capacitors, J. Solid State Electrochem. 23 (2019) 667–692, doi:10.1007/s10008-018-4160-3.

[3] X. Li, J. Yu, S. Wageh, A.A. Al-Ghamdi, J. Xie, Graphene in photocatalysis: a review, Small 12 (2016) 6640–6696, doi:10.1002/smll.201600382.

[4] M. Cruz, C. Gómez, C.J. Duran-Valle, L.M. Pastrana-Martínez, J.L. Faria, A.M.T. Silva, M. Faraldos, A. Bahamonde, Bare TiO$_2$ and graphene oxide TiO$_2$ photocatalysts on the degradation of selected pesticides and influence of the water matrix, Appl. Surf. Sci. 416 (2017) 1013–1021, doi:10.1016/j.apsusc.2015.09.268.

[5] G. Ramalingam, N. Perumal, A.K. Priya, S. Rajendran, A review of graphene-based semiconductors for photocatalytic degradation of pollutants in wastewater, Chemosphere 300 (2022) 134391, doi:10.1016/j.chemosphere.2022.134391.

[6] K. Sheoran, H. Kaur, S.S. Siwal, A.K. Saini, Dai-Viet N. Voc, Vijay Kumar Thakur, Recent advances of carbon-based nanomaterials (CBNMs) for wastewater treatment: synthesis and application, Chemosphere 299 (2022) 134364, doi:10.1016/j.chemosphere.2022.134364.

[7] X. Li, G. Zhang, X. Bai, X. Sun, X. Wang, E. Wang, H. Dai, Highly conducting graphene sheets and Langmuir–Blodgett films, Nat. Nanotechnol. 3 (2008) 538–542, doi:10.1038/nnano.2008.210.

[8] S. Biswas, L.T. Drzal, A novel approach to create a highly ordered monolayer film of graphene nanosheets at the liquid–liquid interface, Nano Lett. 9 (2009) 167–172, doi:10.1021/nl802724f.

[9] G. Shi, S. Araby, C.T. Gibson, Q. Meng, S. Zhu, J. Ma, Graphene platelets and their polymer composites: fabrication, structure, properties, and applications, Adv. Funct. Mater. 28 (2018) 1–44, doi:10.1002/adfm.201706705.

[10] F. Wang, L.T. Drzal, Y. Qin, Z. Huang, Mechanical properties and thermal conductivity of graphene nanoplatelet/epoxy composites, J. Mater. Sci. 50 (2015) 1082–1109, doi:10.1007/s10853-014-8665-6.

[11] (a) C. Knick, Modeling the exfoliation rate of graphene nanoplatelet production and application for hydrogen storage Wright State University, USA, 2012. Ph.D. Thesishttps://corescholar.libraries.wright.edu/etd_all/628;
(b) O.V. Pupysheva, A.A. Farajian, C.R. Knick, A. Zhamu, B.Z. Jang, Modeling direct exfoliation of nanoscale graphene platelets, 2010 *J. Phys. Chem.* C, 114 21083–21087, doi:10.1021/jp1071378.

[12] H.M. Chong, S.J. Hinder, A.C. Taylor, Graphene nanoplatelet-modified epoxy: effect of aspect ratio and surface functionality on mechanical properties and toughening mechanisms, J. Mater. Sci. 51 (2016) 8764–8790, doi:10.1007/s10853-016-0160-9.

[13] P. Cataldi, A. Athanassiou, I.S. Bayer, Graphene nanoplatelets-based advanced materials and recent progress in sustainable applications, Appl. Sci. 8 (2018) 1438, doi:10.3390/app8091438.

[14] M.M. Nur Nasyifa, A.R. Ruslinda, N.H. Abdul Halim, A.S. Zainol Abidin, F.N. Mohd Faudzi, N.A. Ahmad, Z. Lockman, B. Rezek, A. Kromka, S.C.B. Gopinath, Immuno-probed graphene nanoplatelets on electrolyte-gated field-effect transistor for stable cortisol quantification in serum, J. Taiwan Inst. Chem. Eng. 117 (2020) 10–18, doi:10.1016/j.jtice.2020.12.008.

[15] M.J.G. Guimarey, J.L. Viesca, A.M. Abdelkader, B. Thomas, A. Hernández Battez, M. Hadfield, Electrochemically exfoliated graphene and molybdenum disulfide nanoplatelets as lubricant additives, J. Mol. Liq. (2021), doi:10.1016/j.molliq.2021.116959.

[16] S. Malik, I.H. Gul, M.M. Baig, Hierarchical MnNiCo ternary metal oxide/graphene nanoplatelets composites as high rated electrode material for supercapacitors, Ceram. Int. 47 (2021) 17008–17014, doi:10.1016/j.ceramint.2021.02.272.

[17] R. Moriche, M. Sánchez, A. Jiménez-Suárez, S.G. Prolongo, A. Ureña, Strain monitoring mechanisms of sensors based on the addition of graphene nanoplatelets into an epoxy matrix, Comp. Sci. Technol. 123 (2016) 65–70, doi:10.1016/j.compscitech.2015.12.002.

[18] A. Saravanan, P. Senthil Kumar, S. Srinivasan, S. Jeevanantham, M. Vishnu, K. Vishal Amith, R. Sruthi, R. Saravanan, Dai-Viet N. Vo, Insights on synthesis and applications of graphene-based materials in wastewater treatment: a review, Chemosphere 298 (2022) 134284, doi:10.1016/j.chemosphere.2022.134284.

[19] D. Dhinasekaran, P. Soundharraj, M. Jagannathan, A.R. Rajendran, S. Rajendran, Hybrid ZnO nanostructures modified graphite electrode as an efficient urea sensor for environmental pollution monitoring, Chemosphere 296 (2022) 133918, doi:10.1016/j.chemosphere.2022.133918.

[20] P. Worajittiphon, K. Pingmuang, B. Inceesungvorn, N. Wetchakun, S. Phanichphant, Enhancing the photocatalytic activity of ZnO nanoparticles for efficient rhodamine B degradation by functionalised graphene nanoplatelets, Ceram. Int. 41 (2015) 1885–1889, doi:10.1016/j.ceramint.2014.09.023.

[21] R.A. Mahmud, A.N. Shafawi, K.Ahmed Ali, L.K. Putri, N.I. Md Rosli, A.R. Mohamed, Graphene nanoplatelets with low defect density as a synergetic adsorbent and electron sink for ZnO in the photocatalytic degradation of Methylene Blue under UV–Vis irradiation, Mater. Res. Bull. 128 (2020) 110876, doi:10.1016/j.materresbull.2020.110876.

[22] C. Zhang, U. Chaudhary, D. Lahiri, A. Godavarty, A. Agarwal, Photocatalytic activity of spark plasma sintered TiO2–graphene nanoplatelet composite, Scr. Mater. 68 (2013) 719–722, doi:10.1016/j.scriptamat.2013.01.012.

[23] M. Israr, J. Iqbal, A. Arshad, P. Gómez-Romero, Sheet-on-sheet like calcium ferrite and graphene nanoplatelets nanocomposite: A multifunctional nanocomposite for high-performance supercapacitor and visible light driven photocatalysis, J. Solid State Chem. 293 (2021) 121646, doi:10.1016/j.jssc.2020.121646.

[24] M. Israr, J. Iqbal, A. Arshad, M. Rani, P. Gómez-Romero, R. Benages, Graphene triggered enhancement in visible-light active photocatalysis as well as in energy storage capacity of (CFO)1-x(GNPs)x nanocomposites, Ceram. Int. 46 (2019) 2630–2639, doi:10.1016/j.ceramint.2019.09.232.

[25] M. Israr, J. Iqbal, A. Arshad, S.O. Aisida, I. Ahmad, A unique ZnFe2O4/graphene nanoplatelets nanocomposite for electrochemical energy storage and efficient visible light driven catalysis for the degradation of organic noxious in wastewater, J. Phys. Chem. Solids. 140 (2020) 109333, doi:10.1016/j.jpcs.2020.109333.

[26] M. Israr, J. Iqbal, A. Arshad, P. Gómez-Romero, R. Benages, Multifunctional MgFe2O4/GNPs nanocomposite: Graphene-promoted visible light driven photocatalytic activity and electrochemical performance of MgFe2O4 nanoparticles, Solid State Sci 110 (2020) 106363, doi:10.1016/j.solidstatesciences.2020.106363.

[27] H. Katsumata, M. Sada, Y. Nakaoka, S. Kaneco, T. Suzuki, K. Ohta, Photocatalytic degradation of diuron in aqueous solution by platinized TiO2, J. Hazard. Mater. 171 (2009) 1081–1087, doi:10.1016/j.jhazmat.2009.06.110.

[28] S. Canna-Michaelidou, A.S. Nicolaou, Evaluation of the genotoxicity potential (by Mutatox (TM) test) of ten pesticides found as water pollutants in Cyprus, Sci. Total Environ. 193 (1996) 27–35, doi:10.1016/S0048-9697(96)05322-3.

[29] W. Zhang, C. Li, R. Li, Sol-gel preparation of TiO2-Al2O3 composite materials

[30] C.S. Yang, Y.J. Wang, M.S. Shih, Y.T. Chang, C.C. Hon, Photocatalytic performance of alumina-incorporated titania composite nanoparticles: Surface area and crystallinity, Appl. Catal. A. 364 (2009) 182–190, doi:10.1016/j.apcata.2009.05.052.

[31] (a) A. Mukhamed'yarova, B.ula I. Gareev, D. Nurgaliev, F. Aliev, A. Vakhin, A Review on the role of amorphous aluminum compounds in catalysis: Avenues of investigation and potential application in petrochemistry and oil refining, 2021 Processes, 9 1811, doi:10.3390/pr9101811;
(b) G. Paglia, Determination of the structure of γ-alumina using empirical and first principes calculations combined with experiments Curtin University of Technology. Australia, 2004. PhD Thesis https://espace.curtin.edu.au/bitstream/handle/20.500.11937/2341/14992_Paglia_Gianluca%202004.pdf?sequence=2&isAllowed=y .

[32] L. Samain, A. Jaworski, M. Edén, D.M. Ladd, D.K. Seo, F.J. Garcia-Garcia, U. Häussermann, Structural analysis of highly porous γ-Al2O3, J. Solid State Chem. 217 (2014) 1–8, doi:10.1016/j.jssc.2014.05.004.

[33] T. Dascalescu, L. Todan, A. Rusu, S. Preda, C. Andronescu, D.C. Culita, C. Munteanu, M. Zaharescu, Nanosized Al2O3-TiO2 oxide powder with enhanced porosity obtained by sol-gel method, Rev. Roum. Chim. 59 (2014) 125–134 https://web.icf.ro/rrch/.

[34] K.A. Cychosz, R. Guillet-Nicolas, J. García-Martínez, M. Thommes, Recent advances in the textural characterization of hierarchically structured nanoporous materials, Chem. Soc. Rev. 46 (2017) 389–414, doi:10.1039/c6cs00391e.

[35] M. Thommes, K. Kaneko, A.V. Neimark, J.P. Olivier, F. Rodriguez-Reinoso, J. Rouquerol, K.S.W. Sing, Physisorption of gases, with special reference to the evaluation of surface area and pore size distribution (IUPAC Technical Report), Pure Appl. Chem 87 (2015) 1051–1069, doi:10.1515/pac-2014-1117.

[36] L. Atanda, A. Shrotri, S. Mukundan, Q. Ma, M. Konarova, J. Beltramini, Direct production of 5-Hydroxymethylfurfural via catalytic conversion of simple and complex sugars over phosphated TiO2, Chem. Sus. Chem. 8 (2015) 2907–2916, doi:10.1002/cssc.201500395.

[37] A.S. Ali, A.J. Mohammed, H.R. Saud, Hydrothermal synthesis of TiO2/Al2O3 nanocomposite and its application as improved sonocatalyst, Int. J. Eng. Technol. 7 (2018) 22–25, doi:10.14419/ijet.v7i4.37.23607.

[38] X. Jin, L. Gao, J. Sun, Y. Liu, L. Gui, Highly transparent AlON pressurelessly sintered from powder synthesized by a novel carbothermal nitridation method, J. Am. Ceram. Soc. 95 (2012) 2801–2807, doi:10.1111/j.1551-2916.2012.05253.x.

[39] M. Farahmandjou, Self-cleaning measurement of nano-sized photoactive TiO2, J. Comput. Robot. 7 (2014) 15–19 https://www.qjcr.ir/article_638.html.

[40] A.S. Poluboyarinov, V.I. Chelpanov, V.A. Lebedev, D.A. Kozlov, K.M. Khazova, D.S. Volkov, I.V. Kolesnik, A.A. Garshev, Titanium oxide microspheres with tunable size and phase composition, Materials 12 (2019) 1472, doi:10.3390/ma12091472.

[41] R. Nawaz, C.F. Kait, H.Y. Chia, M.H. Isa, L.W. Huei, Glycerol-mediated facile synthesis of colored titania nanoparticles for visible light photodegradation of phenolic compounds, Nanomaterials 9 (2019) 1–19, doi:10.3390/nano9111586.

[42] F. Sordello, G. Zeb, K. Hu, P. Calza, C. Minero, T. Szkopek, M. Cerrut, Tuning TiO2 nanoparticle morphology in graphene–TiO2 hybrids by graphene surface modification, Nanoscale 6 (2014) 6710–6719, doi:10.1039/c4nr01322k.

[43] X. Wang, S.M. Tabakman, H. Dai, Atomic Layer Deposition of Metal oxides on pristine and functionalized graphene, J. Am. Chem. Soc. 130 (2008) 8152–8153, doi:10.1021/ja8023059.

[44] K. Kim, H.-B.-R. Lee, R.W. Johnson, J.T. Tanskanen, N. Liu, M.G. Kim, C. Pang, C. Ahn, S.F. Bent, Z. Bao, Selective metal deposition at graphene line defects by atomic layer deposition, Nat. Commun. 5 (2014) 4781, doi:10.1038/ncomms5781.

[45] M.F. Mazza, M. Cabán-Acevedo, H.J. Fu, M.C. Meier, A.C. Thompson, Z.P. Ifkovits, A.I. Carim, N.S. Lewis, Selective-area, water-free atomic layer deposition of metal oxides on graphene defects, *ACS Mater. Au* 2 (2022) 74–78, doi:10.1021/acsmaterialsau.1c00049.

[46] B. Bharti, S. Kumar, H.N. Lee, R. Kumar, Formation of oxygen vacancies and Ti3+ state in TiO2 thin film and enhanced optical properties by air plasma treatment, Sci. Rep. 6 (2016) 1–12, doi:10.1038/srep32355.

[47] (a) W.C. Peng, Y.C. Chen, J.L. He, S.L. Ou, R.H. Horng, D.S. Wuu, Tunability of p- and n-channel TiOx thin film transistors, Sci. Rep. 8 (2018) 1–11, doi:10.1038/s41598-018-27598-5; (b) M. Janczarek, E. Kowalska, Defective dopant-free TiO2 as an efficient visible light-active photocatalyst, Catalysts 11 (2021) 978, doi:10.3390/catal11080978.

[48] X. Wang, H. Liu, L. Zhao, Y. Wang, S. Wang, Improved resistive switching characteristics of atomic layer deposited Al2O3/La2O3/Al2O3 multi-stacked films with Al+ implantation, J. Mater. Sci. Mater. Electron. 30 (2019) 12577–12583, doi:10.1007/s10854-019-01618-0.

[49] Y. Wang, M. Lei, Q. Wei, Y. Wang, J. Zhang, Y. Guo, J. Saroia, 3D printing biocompatible l-Arg/GNPs/PLA nanocomposites with enhanced mechanical property and thermal stability, J. Mater. Sci. 55 (2020) 5064–5078, doi:10.1007/s10853-020-04353-8.

[50] B. Lesiak, L. Kövér, J. Tóth, J. Zemek, P. Jiricek, A. Kromka, N. Rangam, C sp2/sp3 hybridisations in carbon nanomaterials–XPS and (X)AES study, Appl. Surf. Sci. 452 (2018) 223–231, doi:10.1016/j.apsusc.2018.04.269.

[51] Q. Wu, H. Zhang, L. Zhou, C. Bao, H. Zhu, Y. Zhang, Synthesis and application of rGO/CoFe2O4 composite for catalytic degradation of methylene blue on heterogeneous Fenton-like oxidation, J. Taiwan Inst. Chem. Eng. 67 (2016) 484–494, doi:10.1016/j.jtice.2016.08.004.

[52] J. Oliva, C. Gómez-Solís, L.A. Diaz-Torres, A. Martines-Luevanos, A.I. Martínez,

A.d.J. Zurita-Yduarte, D.J. Gallegos-Hernández, U.A. Sierra-Gómez et al.

Carbon Trends 9 (2022) 100213

E. Coutino-González, Photocatalytic hydrogen evolution by flexible graphene composites decorated with Ni(OH)$_2$ nanoparticles, J. Phys. Chem. C 122 (2018) 1477–1485, doi:10.1021/acs.jpcc.7b10375.

[53] C. Gómez-Solís, J.C. Ballesteros, L.M. Torres-Martínez, I. Juárez-Ramírez, RuO$_2$-NaTaO$_3$ heterostructure for its application in photoelectrochemical water splitting under simulated sunlight illumination, Fuel 166 (2016) 36–41, doi:10.1016/j.fuel.2015.10.104.

[54] A.A. Yadav, Y.M. Hunge, S.B. Kulkarni, Synthesis of multifunctional FeCo$_2$O$_4$ electrode using ultrasonic treatment for photocatalysis and energy storage applications, Ultrason. Sonochem. 58 (2019) 104663, doi:10.1016/j.ultsonch.2019.104663.

[55] Y. Zhang, N. Zhang, Z.R. Tang, Y.J. Xu, Improving the photocatalytic performance of graphene-TiO$_2$ nanocomposites via a combined strategy of decreasing defects of graphene and increasing interfacial contact, Phys. Chem. Chem. Phys. 14 (2012) 9167–9175, doi:10.1039/c2cp41318c.

[56] A. Kumar, P. Raizada, P. Singh, R.V. Saini, A.K. Saini, A. Hosseini-Bandegharaei, Perspective and status of polymeric graphitic carbon nitride based Z-scheme photocatalytic systems for sustainable photocatalytic water purification, Chem. Eng. J. 391 (2020) 123496, doi:10.1016/j.cej.2019.123496.